Determination of cloud transmittance for all sky imager based solar nowcasting

B. Nouri[1], S. Wilbert[1], L. Segura[1], P. Kuhn[1], N. Hanrieder[1], A. Kazantzidis[2], T. Schmidt[3], L. Zarzalejo[4], P. Blanc[5], R. Pitz-Paal[6]

[1]German Aerospace Center (DLR), Institute of Solar Research, Plataforma Solar de Almería (CIEMAT), 04200 Tabernas, Spain

[2]Laboratory of Atmospheric Physics, Department of Physics, University of Patras, 26500 Patras, Greece

[3]DLR, Institute of Networked Energy Systems, Carl-von-Ossietzky-Straße 15, 26129 Oldenburg, Germany

[4]CIEMAT Energy Department – Renewable Energy Division, Av. Complutense 40, 28040 Madrid, Spain

[5]MINES ParisTech, 06904 Sophia Antipolis CEDEX, France

[6]DLR, Institute of Solar Research, Linder Höhe, 51147 Cologne, Germany

Abstract

The demand for accurate solar irradiance nowcast increases together with the rapidly growing share of solar energy within our electricity grids. Intra-hour variabilities, mainly caused by clouds, have a significant impact on solar power plant dispatch and thus on electricity grids. All sky imager (ASI) based nowcasting systems, with a high temporal and spatial resolution, can provide irradiance nowcasts that can help to optimize CSP plant operation, solar power plant dispatch and grid operation. The radiative effect of clouds is highly variable and depends on micro- and macrophysical cloud properties. Frequently, nowcasting systems have to measure/estimate the radiative effect during complex multi-layer conditions with strong variations of the optical properties between individual clouds.

We present a novel approach determining cloud transmittance from measurements or from correlations of transmittance with cloud height information. The cloud transmittance is measured by a pyrheliometer when shaded, as the ratio of shaded direct normal irradiance (DNI) and clear sky DNI. However, for most clouds, direct transmittance measurements are not available, as these clouds are not shading the used pyrheliometers. These clouds receive an estimated transmittance value based on (1) their height, (2) results of a probability analysis with historical cloud height and transmittance measurements as well as (3) recent transmittance measurements and their corresponding cloud height. Cloud heights are measured by a stereoscopic approach utilizing two ASIs. We discuss site dependencies of the presented transmittance estimation method and the potential integration of automatic cloud classification approaches.

We validated the cloud transmittance estimation over two years (2016 and 2017) and compare the probabilistic cloud transmittance estimation approach with four simple approaches. The

overall mean-absolute deviation (MAD) and root-mean-square deviation (RMSD) are 0.11 and 0.16 respectively for transmittance. The deviations are significantly lower for optically thick or thin clouds and larger for clouds with moderate transmittance between 0.18 and 0.585.

Furthermore we validated the overall DNI forecast quality of the entire nowcasting system, using this transmittance estimation method, over the same data set with three spatially distributed pyrheliometers. Overall deviations of 13% and 21% are reached for the relative MAD and RMSD with a lead time of 10 minutes. The effects of the chosen data set on the validation results are demonstrated by means of the skill score.

Keywords

Nowcasting, cloud properties, optical thickness, transmittance, all sky imager, irradiance map

1 Introduction

1.1 Motivation and state of the art

Substantial price drops especially in photovoltaic (PV) but also in concentrating solar thermal power (CSP) generation lead to a notable growth of the total share of solar energy within our grids. Estimations for the total global PV electricity contributions for the year 2030 vary largely from 4.1% to 15.9% (**Breyer et al. 2017**). However, the variable nature of the incoming downward shortwave solar radiation impacts the dispatched solar electricity and poses operational challenges for CSP plants (**Hirsch et al. 2014**) as well as electricity grids (**Perez et al. 2016**). Attenuation in clouds induces the strongest contribution of intra-hour variability (**Schroedter-Homscheidt et al. 2018**). The magnitude of solar irradiance scattering and absorption, causing the attenuation, depends on various micro- and macrophysical properties of the clouds (**Hess et al. 1998**). The solar irradiance arriving on the ground can be predicted by forecasting systems, which observe and analyze the present cloud cover. Intra-hour solar irradiance forecast could be used to reduce needed backup/storage capacities (**Chen et al. 2017**) and optimize the operation of CSP power plants (**Noureldin et al. 2017**) and electricity grids (**Inman et al. 2013**).

Due to current temporal and spatial resolution constrains, satellite based systems and numerical weather models are not suitable for intra-hour forecast (**Schroedter-Homscheidt & Gesell 2016; Lorenz et al. 2009**). All sky imager (ASI) systems can provide the required temporal and spatial resolution for such short-term intra-hour forecasts.

ASI based nowcasting systems detect clouds in the sky images, geolocate them, identify their motion and analyze their radiative effect. Cloud detection algorithms can be based on a set of

fixed thresholds applied to the images' RGB values (e.g. **Heinle et al. 2010; Kazantzidis et al. 2012)**, clear sky libraries (e.g. **Chow et al. 2011; Wilbert et al. 2016a**) or machine learning approaches (e.g. **Taravat et al. 2015; Ye et al. 2017**). Geolocation of clouds can be achieved by stereoscopic approaches (e.g. **Nguyen et al. 2014; Blanc et al. 2017; Kazantzidis et al. 2017**) or by introducing additional supplementary remote sensing of cloud heights (e.g. **Schmidt et al. 2016; Richardson et al. 2017**). The most widely used cloud tracking approaches are based on block matching (e.g. **Nguyen et al. 2014; Blanc et al. 2017; Kazantzidis et al. 2017**) or optical flow algorithms (e.g. **Huang et al. 2012; West et al. 2014; Chow et al. 2015**). The radiative effect of clouds can be analyzed by radiative transfer models. **Mejia et al. 2016** couples synthetic overcast sky images with a radiative transfer model and estimates the cloud optical thickness from the images. **Tzoumanikas et al. 2016** classifies the dominant cloud type from ASI images and studies the radiative effect by a radiative transfer model and aerosol information gathered by a Cimel sun photometer. Another option to analyze the radiative effect, are numerous spatially distributed solar irradiance measurements on the ground (e.g. **Schmidt et al. 2016**).

1.2 Objective of presented work

In previous publications we presented and validated a nowcasting system with individual cloud objects (**Nouri et al. 2018, Kuhn et al. 2017**). Each cloud object receives corresponding attributes such as height, position, motion and transmittance. The image processing consists of the cloud segmentation with a four dimensional clear sky library (**Wilbert et al. 2016a**), stereoscopic cloud geolocation (**Nouri et al. 2019**), a block matching cloud tracking approach (**Nouri et al. 2019**) and the cloud transmittance estimation approach, which is the main topic of this paper. Finally spatial DNI maps with lead times up to 15 minutes ahead in steps of 1 minute and edge lengths of 8 km are created (**Nouri et al. 2018**). Also global horizontal irradiance (GHI)

maps and global tilted irradiance (GTI) maps can be created, but this is not the scope of this work. We present a probabilistic cloud transmittance estimation method, based on historical and recent cloud height and transmittance measurements. The required cloud height is measured with a stereoscopic method described in **Nouri et al. 2019.** The transmittance of clouds (T) for the instrument specific field of view can be measured by ground based pyrheliometer (**Raschke & Cox 1983**; **Zangvil & Lamb 1997**), as the ratio of shaded (I_{sh}) and clear sky irradiance (I_{cl}) according to Equation 1.

$$T = I_{sh}/I_{cl} \quad \textbf{Equation 1}$$

In this work, the attenuation of the direct solar beam is measured with a CHP1 Kipp&Zonen pyrheliometer (5° field of view). For the determination of the clear sky DNI, the Linke turbidity is calculated from DNI measurements according to **Ineichen & Perez 2002**. Shaded DNI measurements are rejected using the method from **Hanrieder et al. 2016** & **Wilbert et al. 2016b**. The current Linke turbidity is calculated by the most recent and unshaded Linke turbidity measurements, weighting more recent measurements stronger. The predicted clear sky DNI is calculated with the current Linke turbidity according to **Ineichen & Perez 2002**. The used clear sky DNI is validated over a two year period (2016 and 2017). An overall relative MAD of roughly 1% is observed, which is considered as acceptable for the nowcasting system.

The used nowcasting system creates irradiance maps with an edge length of 8 km and forecasts up to 15 minutes ahead. Various clouds detected by the ASIs might cast a shadow on the observed area within the next 15 minutes. The angular distance of relevant clouds to the sun as seen depends on the cloud height and speed. For some of these clouds a transmittance measurement might be available, but for many clouds the transmittance cannot be measured directly (see Figure 1). A homogenous average transmittance, corresponding to the last

measured transmittance values, for all visible clouds might be acceptable as a first approximation during single-layer conditions. However, this approach would lead to increased uncertainties during complex but frequent multi-layer conditions (**Wang et al. 2000; Li et al 2011**). Therefore, an extended transmittance allocation approach is needed.

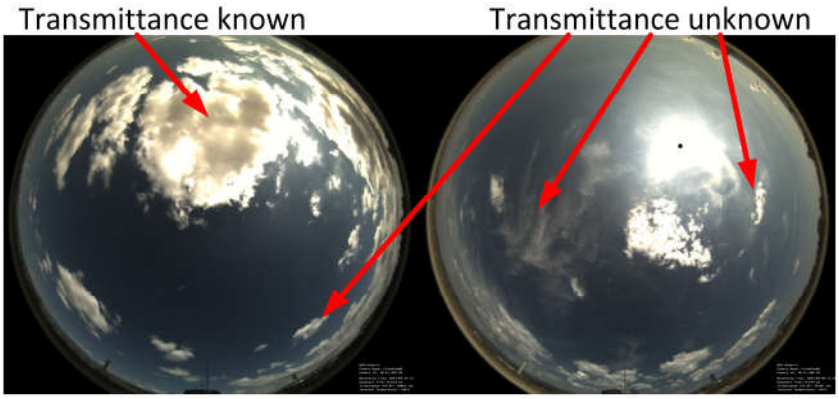

Figure 1: Sky images of an ASI located in close proximity to a pyrheliometer (Left) single-layer day (Right) multi-layer day with different cloud types.

1.3 Radiative effect of different cloud classes and cloud height layers

A probabilistic approach is chosen which is motivated by two facts. Firstly vertical cloud profiles hold important information for distinct cloud types (**Frederick & Steele 1995; Wang & Sassen 2001; Kahn et al. 2008**). In general the troposphere is discretized into a lower, middle and high layer. Cumulus (Cu), stratus (St) and stratocumulus (Sc) clouds are associated to the lower layer, altocumulus (Ac) and altostratus (As) to the middle layer and cirrus (Ci), cirrocumulus (Cc) and cirrostratus (Cs) to the higher layer (**Rossow & Schiffer 1999**). Vertical thick clouds like nimbostratus (Ns) and deep convective clouds can extend over all three layers. The heights of the borders between these layers are not static and dependent on latitude (**Manabe 1969; Ohring & Adler 1978; Sassen & Wang 2012**). **Sassen & Wang 2012** divide the earth in the three latitude belts, polar, mid-latitude and tropics (see Table 1), with corresponding borders between the three layers.

Table 1: Borders of troposphere low, middle and upper layer for the three latitude belts polar, mid-latitude and tropics as defined by Sassen & Wang 2012 (values in brackets describe transition zone between layers)

	Low layer	Middle layer	high layer
Polar (> 66°33' north and south)	0 km < h ≤ 1.8 km (2.4 km)	(1.8 km) 2.4 km < h ≤ 5.0 km (7.0 km)	h > (5.0 km) 7.0 km
Mid-latitude (23°26' to 66°33' north and south)	0 km < h ≤ 1.8 km (2.4 km)	(1.8 km) 2.4 km < h ≤ 6.0 km (8.0 km)	h > (6.0 km) 8.0 km
Tropics (< 23°26' north and south)	0 km < h ≤ 1.8 km (2.4 km)	(1.8 km) 2.4 km < h ≤ 7.0 km (10.0 km)	h > (7.0 km) 10.0 km

The second fact motivating the probabilistic approach is that different cloud types can be associated to different optical properties (**Chen et al. 2000**). Solar irradiance is attenuated in the atmosphere by absorption and scattering. The attenuation caused by clouds is described by the cloud optical thickness (COT). The COT of a cloud depends on micro- and macrophysical properties such as particle size distribution, shape, water path (WP), thermodynamic phase and vertical extent (**King 1987**; **Hess et al. 1998; Chen et al. 2000; Kokhanovsky 2004**). Especially WP, which describes the vertically integrated water content (WC), and effective particle size are proportional to COT (**Lohmann & Neubauer 2018**). The average global WP of low and middle layer clouds is significantly larger than compared to high layer clouds (**Rossow & Schiffer 1999**). Larger effective particle size leads to stronger absorptance whereas smaller effective particle size increases the scattering (**Chang& Li 2002**). **Rossow & Schiffer 1999** used within International Satellite Cloud Climatology Project (ISCCP) nine cloud types discretized by cloud top pressure and COT. **Hahn et al. 2001** relate ISCCP data to visual observations from the ground and reduce the ISCCP cloud type definition to four distinguishable types: all low layer clouds (Cu, Sc, St and fog), optically thin middle layer clouds (Ac and thin As), cirrus clouds (Ci, Cs and Cc) and thick high –topped clouds (cumulonimbus (Cb), Ns and thick As). The ISCCP data set states the lowest average COT with 2.2 for the cirrus clouds. Cirrus clouds consist almost exclusively of nonspherical ice crystals of various shapes (**Fu 1996**). The optical properties differ significantly between ice crystals and spherical liquid drops. The extinction

coefficients of water clouds are one or two orders of magnitude greater than those of ice clouds with the same WP (**Sun & Shine 1994**). The effective particle size is at least one order of magnitude greater for ice particle compared to liquid particle with the same WC. Thus, the chance of multiple scattering is greater for water clouds (**Sun & Shine 1994**). In more recent studies with combined radar and lidar as well as CloudSat and CALIPSO measurements, the global average COT of ice clouds are found around 1 with an ice WP of 25 gm^{-2} (**Hong & Liu 2016**). The radiative properties of mixed phased clouds have to be considered too. Low layer and middle layer clouds are often considered as purely liquid clouds and high layer clouds as ice clouds. The reality is somewhat more complex. Clouds with temperatures above 0°C consist of liquid particles and clouds with temperatures below -40°C consist of ice particles. However, in between clouds may consist of supercooled liquid particles, ice particles or a mixture (**Pruppacher & Klett 1997**). Around 30% of all clouds within the temperature range of -8°C and -26°C consist of mixed phase clouds (**Sun & Shine 1994**). The related strong variation of the optical thickness can be described roughly by a linear function of the ice fraction, with optically thicker liquid dominated clouds to optically thinner ice dominated clouds (**Sun & Shine 1994**). Especially clouds from the middle troposphere layer have temperatures associated with mixed phase clouds. Ac clouds are liquid dominated and As clouds ice dominated (**Sassen & Wang 2012**)**.**

There is no simple relation between cloud height, type and optical thickness, due to the highly variable micro- and macrophysical nature of clouds. However, a tendency exists for mainly optically thick low layer liquid clouds, optically moderate to thick middle layer clouds and optically thin high layer ice clouds. Therefore, a probabilistic approach, including historical and current cloud height and transmittance measurements (see Figure 2), seems feasible to relate cloud height and transmittance for cloud transmittance estimations (if needed).

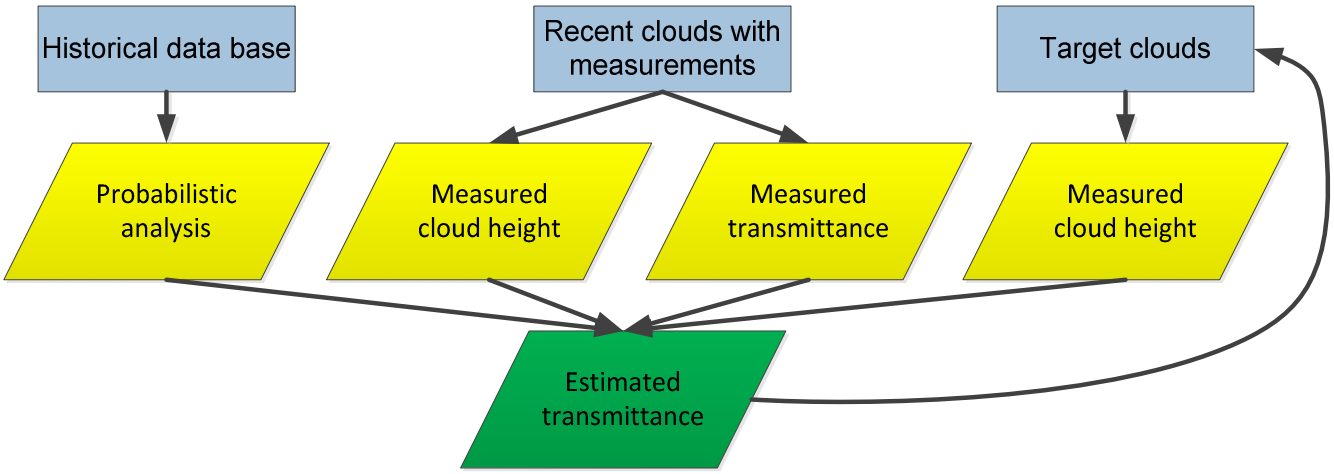

Figure 2: Rough structure of probabilistic cloud transmittance estimation approach

Section 2 of this paper presents the nowcasting and validation test set up. Section 3 describes the transmittance estimation and allocation method. The results of a validation with a data set of two years are presented in section 4. Site dependencies of the presented approach as well as the potential of an automatic cloud classification for the improvement of the used transmittance estimation method are discussed in section 5. The conclusion is given in section 6.

2 Nowcasting and validation instrumentation and data

The nowcasting system used in this study consists of two ASIs (Mobotix Q24 surveillance cameras) and one CHP1 pyrheliometer. The DNI data quality check is done according to **Geuder et al. 2015**. The cameras and pyrheliometer are cleaned each weekday. Hemispherical sky images are taken every 30 s.

The studied nowcasting system is located at the Plataforma Solar de Almería (PSA) in southern Spain (latitude: 37.09° (north) and longitude: -2.36° (east) see Figure 3). Two additional reference pyrheliometers, used for the forecast validation, are placed north of the cameras (see Figure 2). Additional cloud base height (CBH) measurements are taken by a CHM 15k Nimbus

ceilometer from the G. Lufft Mess- und Regeltechnik GmbH. The ceilometer data are used for the probability analysis described in section 3.

574 cloudy days distributed over the years 2014 to 2017 are used for the probability analysis. A total of 316419 valid transmittance measurements are detected within this data set. The complete years 2016 and 2017 are used for the validation (see section 4) of the transmittance estimation method. The data set of the probability analysis and the data set of the validation data set have no overlap. The probability analysis data set considers only data samples with transmittance measurements, whereas the validation data set considers only data sample with estimated transmittance values.

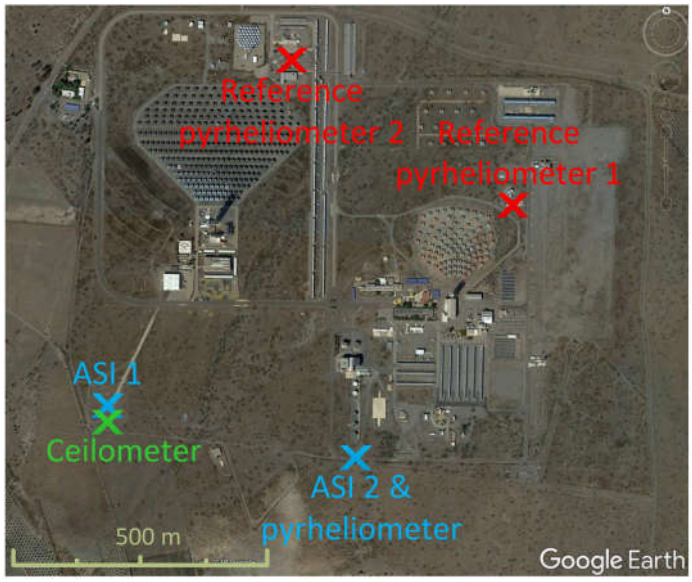

Figure 3: Aerial image of PSA with markers for the ASIs, pyrheliometer and ceilometer (Source: Google Earth [Accessed: 05.05.2018]).

3 Determination of cloud transmittance

3.1 Analysis of the relation between cloud height and transmittance

The nowcasting system treats clouds as individual objects with universal constant properties within a single cloud. However, real clouds consist of complex inhomogeneous structures with horizontal (**Titov 1998; Madhavan et al. 2016**) and vertical (**Chang and Li 2002; Kikuchi et al. 2006**) variabilities, which affect the optical properties. Moreover, cloud boundaries are not clear. **Koren et al. 2007** describes a so-called twilight zone around the clouds. This twilight zone can extend tens of kilometers away from the clouds and consist of cloud fragments and hydrated aerosols. **Bar-Or et al. 2010** differentiates the sky in cloud free and cloud field, where the cloud field consists of the clouds and the twilight zone with corresponding cloud properties. This spatial uncertainty of cloud boundaries is reflected by DNI measurements, making unambiguous transmittance measurements frequently challenging. However, reliable transmittance measurements are needed for the probability analysis. To study stable transmittance measurements DNI measurements with a temporal resolution of 5 s are used. Transmittance measurements are only considered if the standard deviation is less or equal 0.05 over a time period of ±20 s. This threshold is determined empirically. Transmittance measurements are compared with cloud heights measured by a ceilometer. Ceilometer measurements are chosen for the probability analysis, as they are considered to be more accurate in comparison to ASI derived cloud heights (**Nouri et al. 2019**), which show especially for higher cloud layers a stronger dispersion. ASI derived cloud height information could be used, but for this study we aim to create a data base with the highest possible accuracies to test the limitations of our cloud estimation approach. Yet, the ceilometer is limited to cloud measurements directly above the sensor. Thus, the cloud height measured by the ceilometer and the cloud transmittance

237 determined by a close by pyrheliometer often do not belong to the same cloud. Therefore, we
238 confine the probability analysis to conditions with constant lowest CBH. We define these
239 conditions as having standard deviations of the ceilometer measurements less or equal to 500 m
240 over a time period of ±15 minutes. Furthermore, measurements are only considered if the sun
241 elevation angle is above 10° as for very small solar elevations the clouds shading the
242 pyrheliometers are far away from the clouds above the ceilometer.

243 The probability analysis is performed on 574 cloudy days between January 2014 and December
244 2017 at PSA. A total of 316419 valid transmittance measurements with single-layer cloud
245 conditions are available. Figure 4 shows the occurrence of cloud height readings as measured
246 by the ceilometer within this time period.

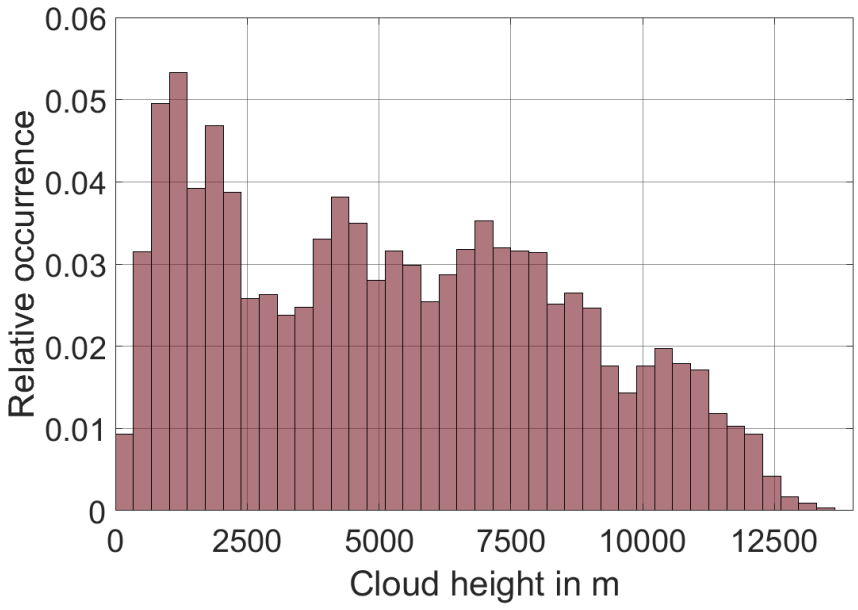

247

248 **Figure 4: Histogram of cloud height readings as measured by the ceilometer used for the probability analysis.**

249 Cloud heights are discretized in five height ranges from 0 to 12.5 km in 2.5 km steps. Readings
250 above 12.5 km are not considered, due to their scarcity (see Figure 4). The lowest range
251 describes all low layer clouds, whereas the second and third layer describes the middle layer

clouds and the last two ranges the high layer clouds. Figure 5 depicts the transmittance measurement distribution over the five height ranges as box plot. The expected increase of transmittance with cloud height is clearly visible. The average transmittance measurements from the lowest to the highest cloud range are 0.06, 0.15, 0.36, 0.52 and 0.68. Especially the lowest height range shows unambiguous results. The moderate middle height range 2.5 to 5.0 km as well as the highest range 10.0 to 12.5 km show a comparatively low variability in transmittance. The 25th and 75th percentile cover a transmittance range of 0.16 and 0.29 respectively. The strongest variabilities in transmittance occur in the height ranges 5.0 to 7.5 km and 7.5 to 10.0 km, with a covered transmittance range by the 25th and 75th percentile of 0.64 and 0.54 respectively.

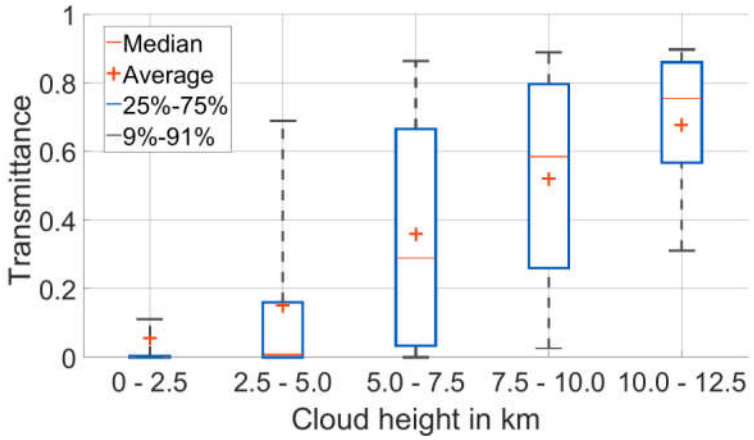

Figure 5: Transmittance readings discretized over cloud heights from 574 cloudy days taken at the PSA.

For the further analysis five arbitrary transmittance ranges from 0 to 0.9 in 0.18 steps are defined. Optically very thin clouds with transmittance above 0.9 are not considered by the nowcasting system. A reliable detection of these optically very thin clouds by the ASIs cannot be assured. The occurrence probability of the defined transmittance range within the height ranges is analyzed for each of the 574 days separately. The box plots in Figure 6 show the probability distribution of transmittance range occurrence within the five height ranges over all days. For the

two lowest height ranges, the average probability for optically very thick clouds ($0 \le T < 0.18$) are 93% ($0 \le h < 2.5$ km) and 77% ($2.5 \le h < 5.0$ km). The remaining transmittance ranges have an average probability below 10%. The height ranges 5.0 to 7.5 km and 7.5 to 10.0 km show the strongest dispersion in probability of transmittance. In the case of the height range 5.0 to 7.5 km the highest average probability remains with the optically very thick clouds (42%). However, the average probability for optically thin clouds ($0.72 \le T \le 0.9$) rises to 21%. An almost inverse situation is observed for the height range 7.5 to 10.0 km, with an average probability of 21% for the optically thick clouds and 34% for the optically thin clouds. For both height ranges the remaining transmittance ranges show a significantly high average probability above 10%. The average probability for thick clouds is quite low with 2% ($0 \le T < 0.18$) and 6% ($0.18 \le T < 0.36$) for the highest cloud height range. On the opposite side of the transmittance spectrum the average probabilities are 23% ($0.54 \le T < 0.72$) and 54% ($0.72 \le T \le 0.9$).

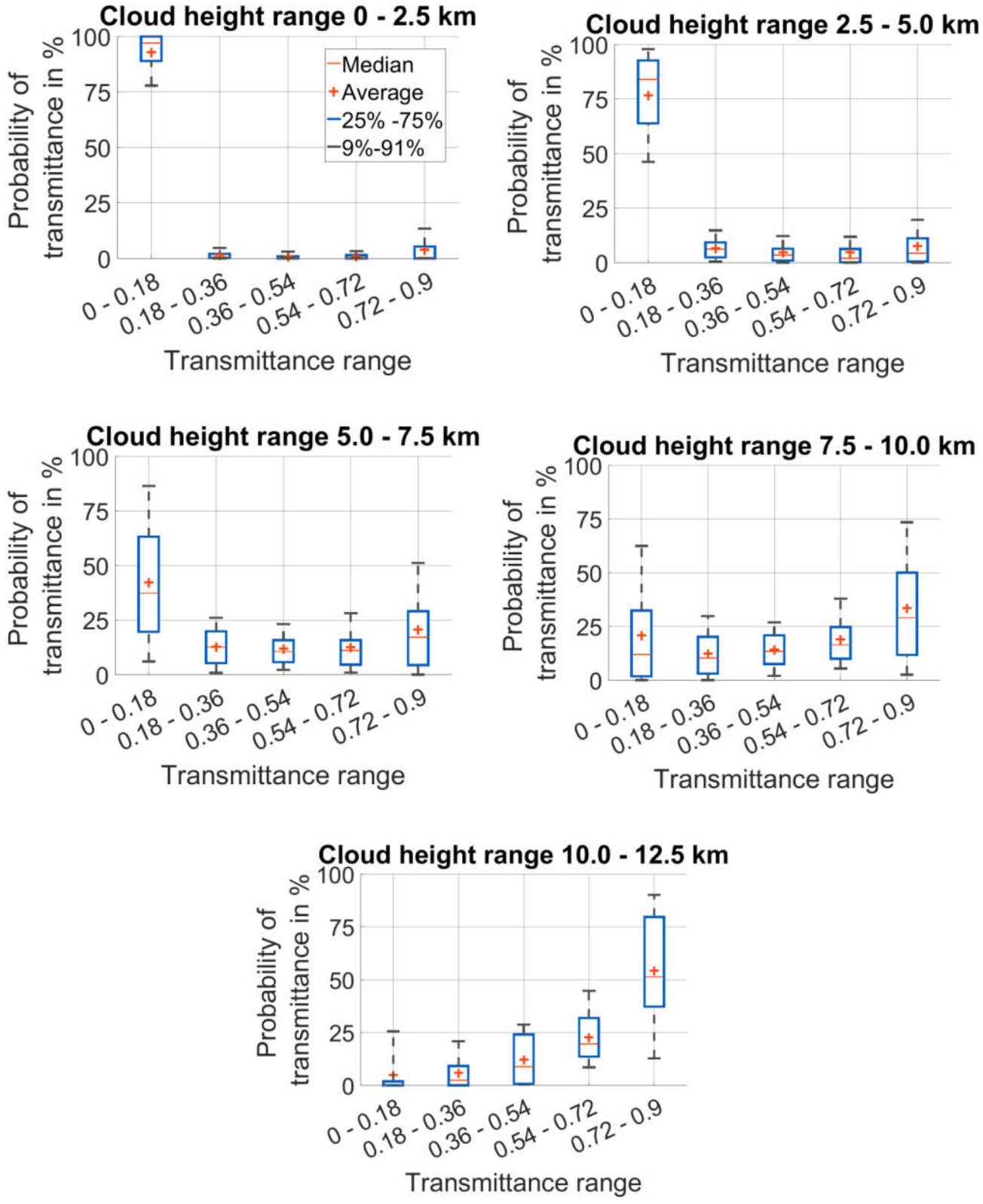

Figure 6: Probability of cloud transmittance occurrence for different cloud transmittance and cloud height ranges from 574 cloudy days taken at the PSA.

3.2 Cloud transmittance estimation method for the nowcasting system

The transmittance estimation for the nowcasting system is based on the ASI derived cloud object specific cloud height. Average relative mean-absolute deviations (MAD) of ≈10%, ≈18% and ≈22% of the ASI cloud heights compared to the ceilometer cloud heights were observed for low layer, middle layer and high layer clouds respectively (**Nouri et al. 2019**). The possible deviation of ASI derived and ceilometer derived cloud heights could lead to erroneous transmittances. These errors are estimated to be acceptable for the method given the distribution of transmittances within each cloud height and the wide height bins. Shadow projection is done individually for each cloud. Thus, the responsible cloud is known together with its corresponding cloud height and transmittance measurement. The nowcasting system saves the recent transmittance measurements and cloud height information in a data base. The transmittances of all detected clouds in the sky without transmittance measurement are determined based on (1) the cloud height, (2) the probability analysis results and (3) recent transmittance measurements. The flow chart for the transmittance estimation method, which explains the method in detail including examples, is shown in Figure 7.

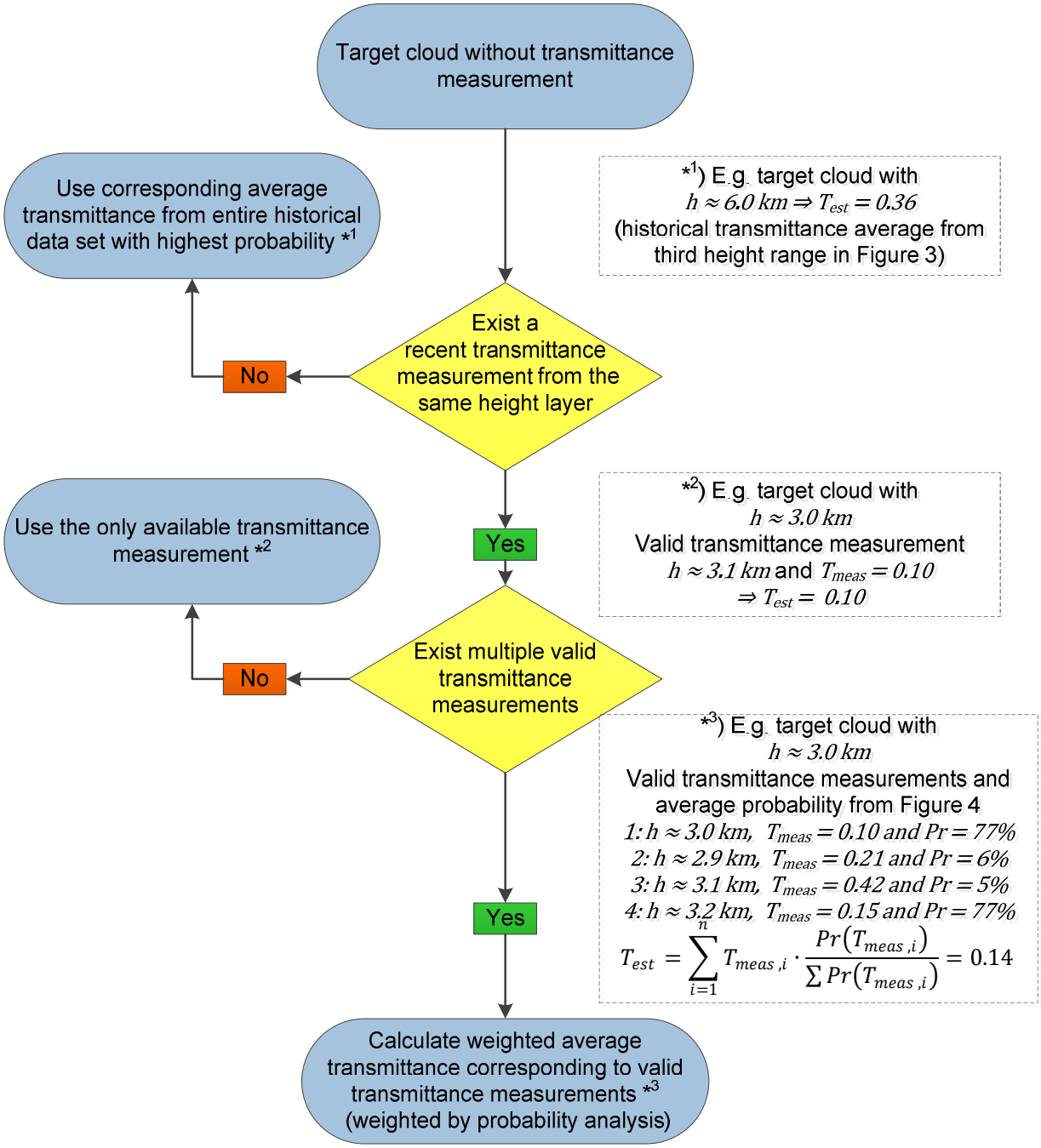

Figure 7: Flowchart for the transmittance estimation with historical results from the probability analysis and recent cloud transmittance and height measurements within the nowcasting system (h: cloud height, T_{meas}: measured transmittance, T_{est}: estimated transmittance and Pr: average probability corresponding to cloud transmittance and cloud height range). Examples of the three options are given marked by *.

4 System validation

4.1 Validation of transmittance estimation approach

Sky images of a two years data set (2016 and 2017) taken at PSA are processed with the nowcasting system including the transmittance estimation approach described in section 3. DNI maps for the current situation and forecasts up to 15 minutes ahead in 1 minute steps are created. Each valid transmittance measurement over the 2 years is saved into a database. Transmittance measurements are gathered in around 14.2% of all processed image series (considering only conditions with clouds). The validation method utilizes all corresponding DNI maps with lead time 0 and 1 minute describing the time stamps of the transmittance measurements. The actual cloud transmittance measurement is applied to the DNI map with a lead time of 0 minute. The clouds responsible for the transmittance measurement received previously to the transmittance measurement a transmittance estimation according to section 3.2, which is known from the DNI map with a lead time of 1 minute (see Figure 8). Thus a comparison between previously estimated and later measured cloud transmittance, corresponding to the same cloud, is possible.

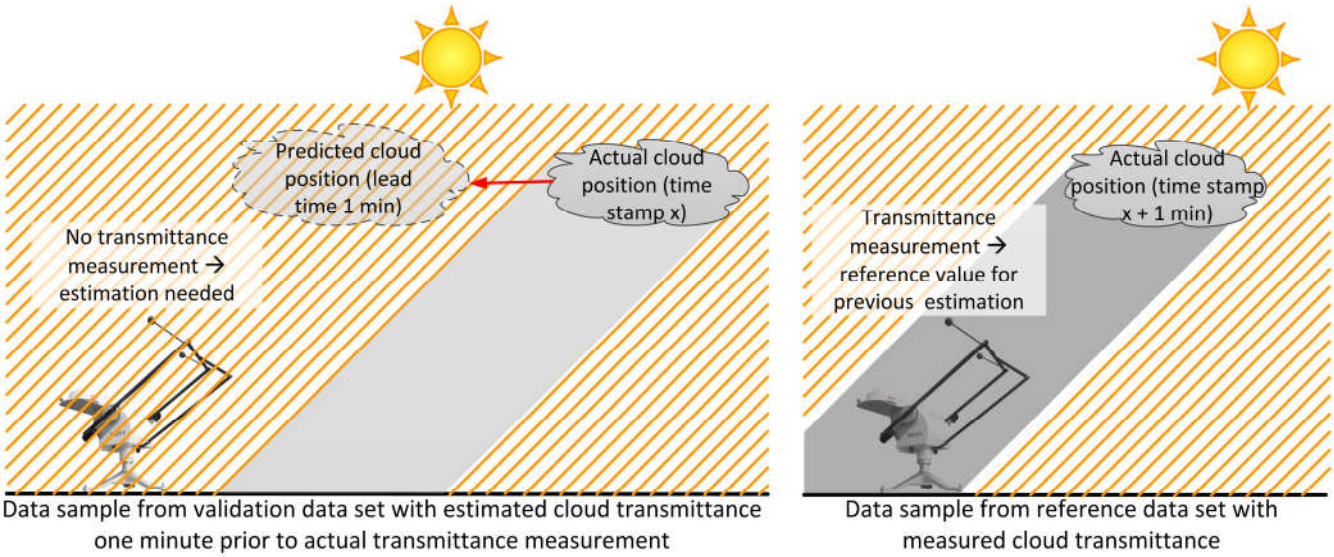

Figure 8: Illustration matching transmittance measurements with previously estimated transmittance values from the same cloud. (Left) cloud with estimated cloud transmittance 1 minute prior to actual transmittance measurement. (Right) Cloud with transmittance measurement.

A scatter density plot is shown in Figure 9. Accumulated relative frequencies of each column add up to 100%. Overall a good agreement is reached with the strongest deviations for the moderate transmittance ranges. A frequent transmittance overestimation is apparent. This is due to two causes. Firstly, the cloud height measurements for the probability analyses are obtained by a ceilometer. As mentioned before, the ceilometer measurements are limited to clouds directly above the sensor. Thus, often the cloud height and cloud transmittance measurements do not belong to the same cloud. This issue is addressed by limiting the data set of the probability analysis to conditions with a constant lowest CBH, assuming quasi constant cloud heights for all visible clouds. This limits the probability analysis almost entirely to single-layer conditions. Multi-layer conditions are only considered in the case of a continuous lowest layer overcast condition, which is a rare case for the PSA. But in general the occurrences of multiple cloud layers are not rare. In a global scale, multi-layer conditions occur in around 42% of all cases (**Wang et al. 2000**). The total attenuation increases with these multi-layer conditions since the direct solar rays have to pass through several cloud layers. The validation period includes

such multi-layer conditions, but receives cloud transmittance estimation corresponding mainly to single-layer conditions. Secondly, the cloud height validation of the nowcasting system detected a tendency for a slight overestimation of the cloud height (**Nouri et al. 2019**), which leads according to the results of the probability analysis to transmittance overestimations.

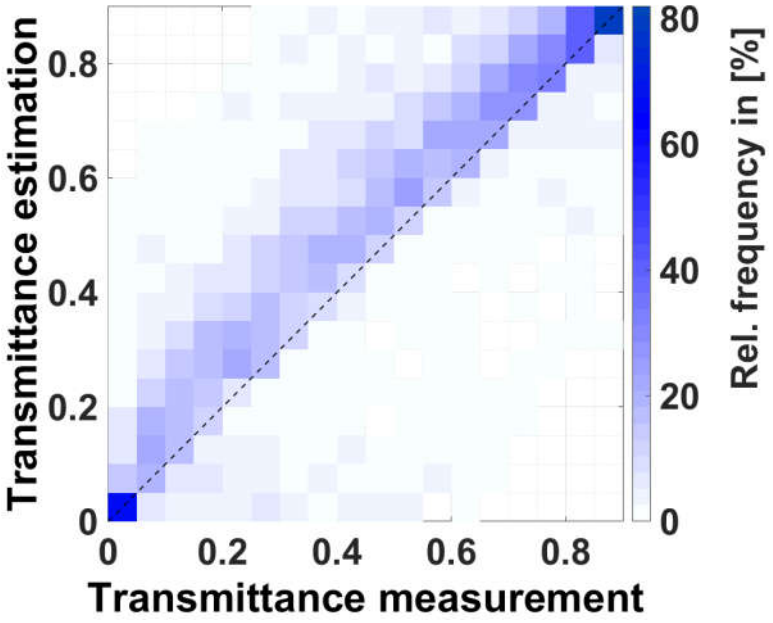

Figure 9: Scatter density plot transmittance estimation over transmittance measurement for the validation data set. The color coding represents the relative frequency for each pixel in a column of the scatter density plot. Accumulated relative frequencies of one column add up to 100%.

Figure 10 shows the MAD and root-mean-square deviation (RMSD) within transmittance ranges (0.045 step size) and the corresponding data density. Nearly 25% of all transmittance measurements belong to the optically very thick clouds with $T \leq 0.045$. Each of the remaining transmittance ranges contains less than 10% of the data. The comparatively high share of optically very thick clouds is partially due to multi-layer conditions, which often attenuate the majority of direct irradiance.

The MAD amounts to 0.06 for the optically very thick clouds and rises to a maximum of 0.20 with $0.315 \leq T < 0.36$. Afterwards the MAD drops down to 0.03 for optically thin clouds with $0.855 \leq T \leq 0.9$. The higher deviations for the moderate transmittance ranges comply with the

results of the probability analysis. The strongest occurrences of the moderate transmittances are found for the middle cloud layer and the lower part of the higher cloud layer up to 10 km (see Figure 5). These are also the layers with the strongest transmittance dispersion. This comes not as a surprise, since especially the middle troposphere covers a wide temperature range, which enables supercooled liquid, ice and mix particle clouds. Thus, the determination of optical properties is more difficult for the middle layer (**Sassen & Wang 2012**; **Kayetha & Collins 2016**).

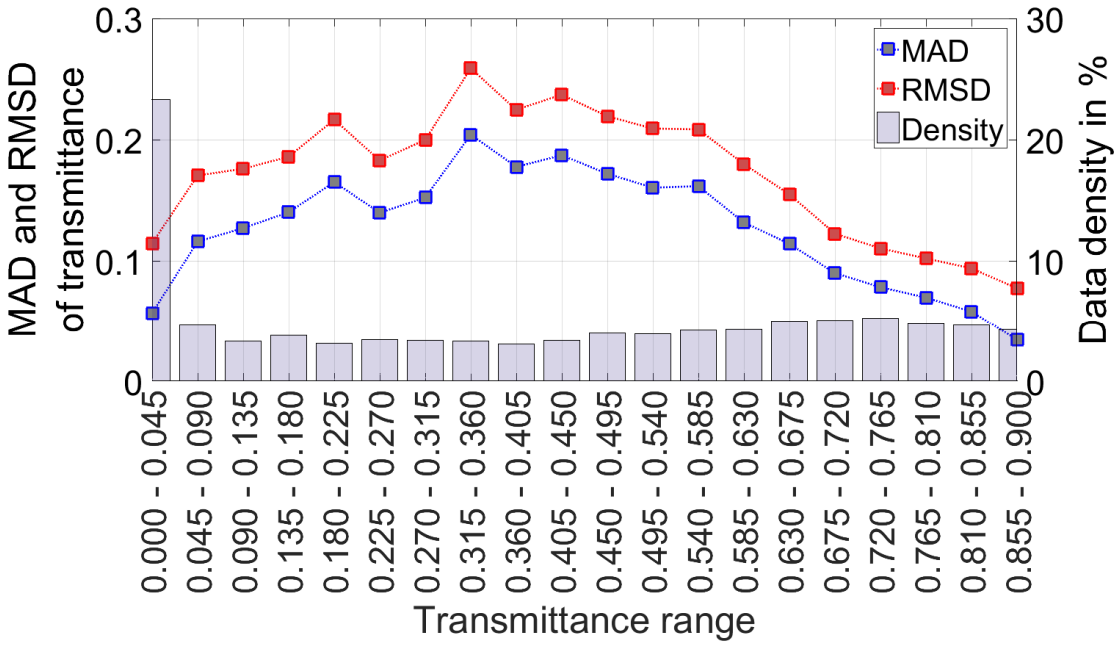

Figure 10: MAD, RMSD and data density over transmittance ranges for the validation data set.

The overall average MAD and RMSD over the entire data set are 0.11 and 0.16 respectively. It has to be pointed out, that these deviations are only relevant if estimates for the transmittance are required. Often consecutive transmittance measurements occur (due to horizontally large clouds/cloud fields), which makes the estimation of clouds transmittance unnecessary for many relevant clouds that shade the target area and leads to a significant reduction of the deviations. This is especially the case for the current conditions and the immediate future of a couple of

379 minutes ahead. For nowcast looking further into the future, the clouds transmittance estimation
380 becomes more important.

381 4.2 Benchmarking of different cloud transmittance approaches

382 In the following we will compare our probabilistic transmittance estimation approach with four
383 more basic transmittance estimation approaches.

384 • Binary approach with a transmittance of 0 for all clouds.
385 • Binary approach with a transmittance of 0.32 for all clouds (average transmittance over
386 entire data set of the probability analysis).
387 • Cloud transmittance estimation according to the average transmittance within the
388 corresponding cloud height bin as given in Figure 5 (This is equivalent to the presented
389 probabilistic approach if no recent transmittance measurements are available).
390 • A persistence approach, which allocates to all clouds a transmittance corresponding to
391 the last measured transmittance.

392 The additional transmittance approaches are validated according to the procedure described in
393 section 4.1. The overall average MAD and RMSD of all approaches are stated in Table 2. The
394 lowest deviations are achieved with the probabilistic approach. The strong deviations of the
395 binary approaches are no surprise, considering the observed distribution in cloud transmittance
396 (see section 3.1). The advantage of the probabilistic approach compared to the remaining
397 approaches can be explained by the combination of historical with recent information, whereas
398 the simple approaches use only historical or recent information.

399

400 **Table 2: Overall MAD and RMSD for different transmittance estimation approaches**

	MAD	RMSD
Probabilistic approach	0.11	0.16
Binary 0	0.39	0.49
Binary 0.32	0.27	0.31
Historical average height dependent	0.24	0.30
Persistence	0.17	0.26

401

402 The deviations discretized over transmittance ranges are illustrated in Figure 11. The binary
403 approaches dominate the bins they are related to, with a linear increasing deviation from these
404 bins. The advantage of the probabilistic approach is most visible for optical very thick or very thin
405 clouds.

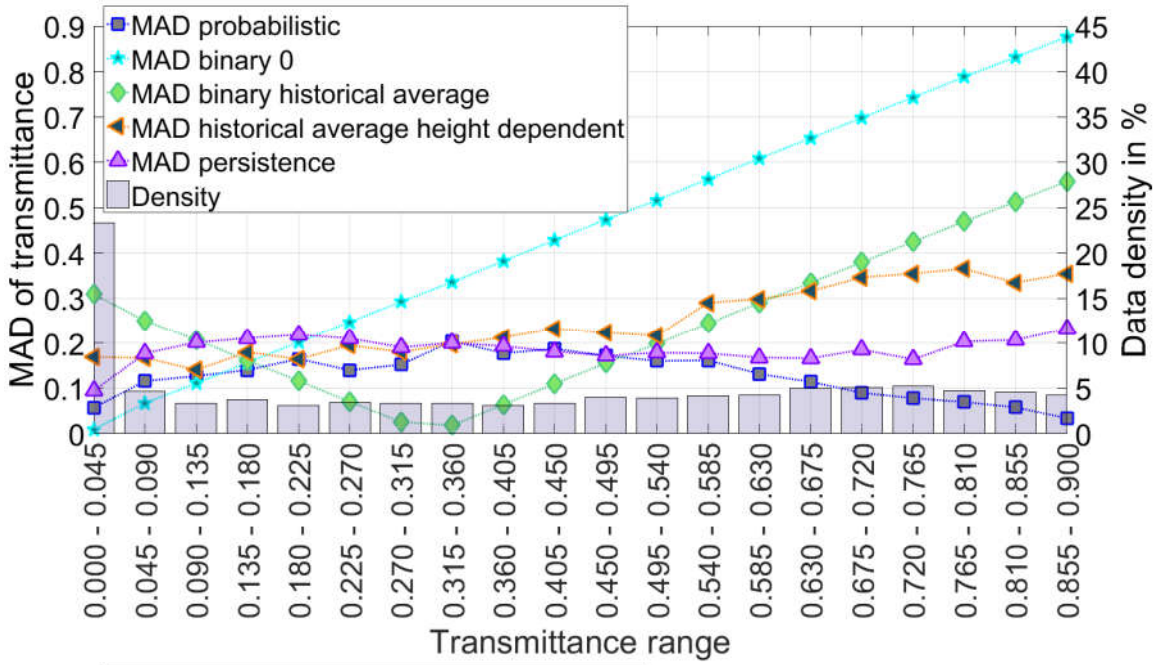

406

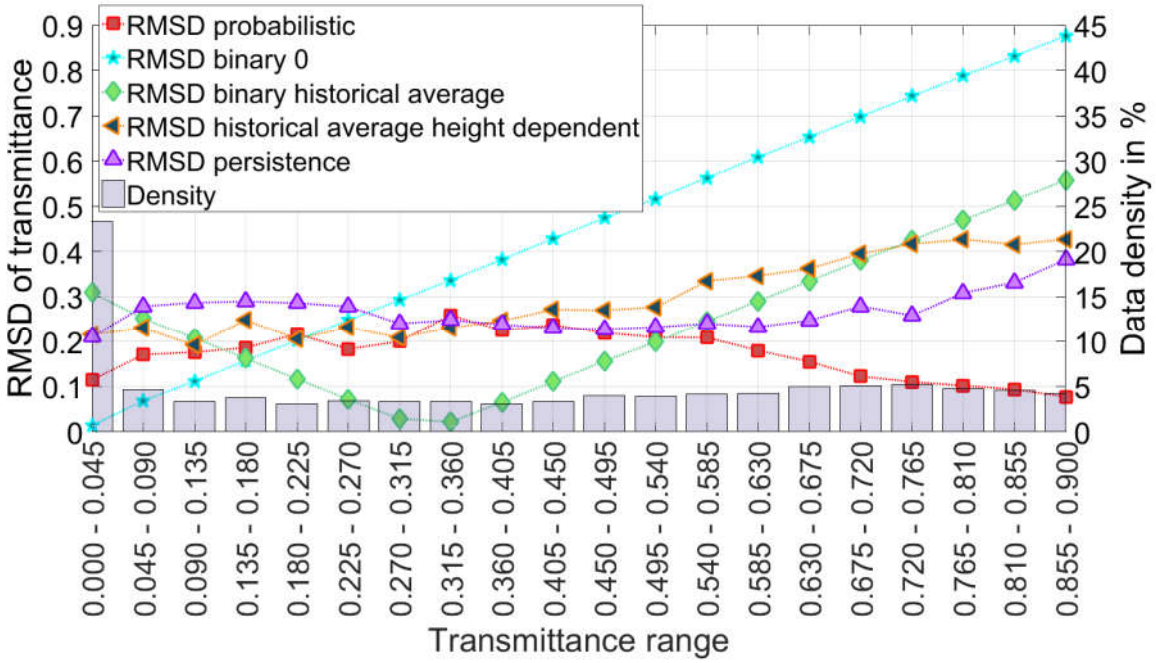

407

408 **Figure 11: MAD, RMSD and data density over transmittance ranges for the validation data set for different transmittance**
409 **estimation approaches**

410

4.3 Validation of DNI forecast

Three reference pyrheliometer are used to validate the overall forecast quality of the irradiance maps, according to the approach described in **Kuhn et al. 2017**. Pixels from the irradiance maps corresponding to pyrheliometer positons are compared to the reference DNI values on 1 minute averages (see Figure 12 (left)). Relative deviation metrics of the validation period (two years) are shown in Figure 12 (right). The relative bias, MAD and RMSD for lead time 0 minutes is approximately 2%, 4% and 8%, respectively, and rises up to 5%, 15% and 23%, respectively, for a lead time of 15. The deviations increase for higher lead times, due to uncertainties of the used tracking and transmittance estimation method. As mentioned before, the transmittance estimations become more important, for predictions further into the future.

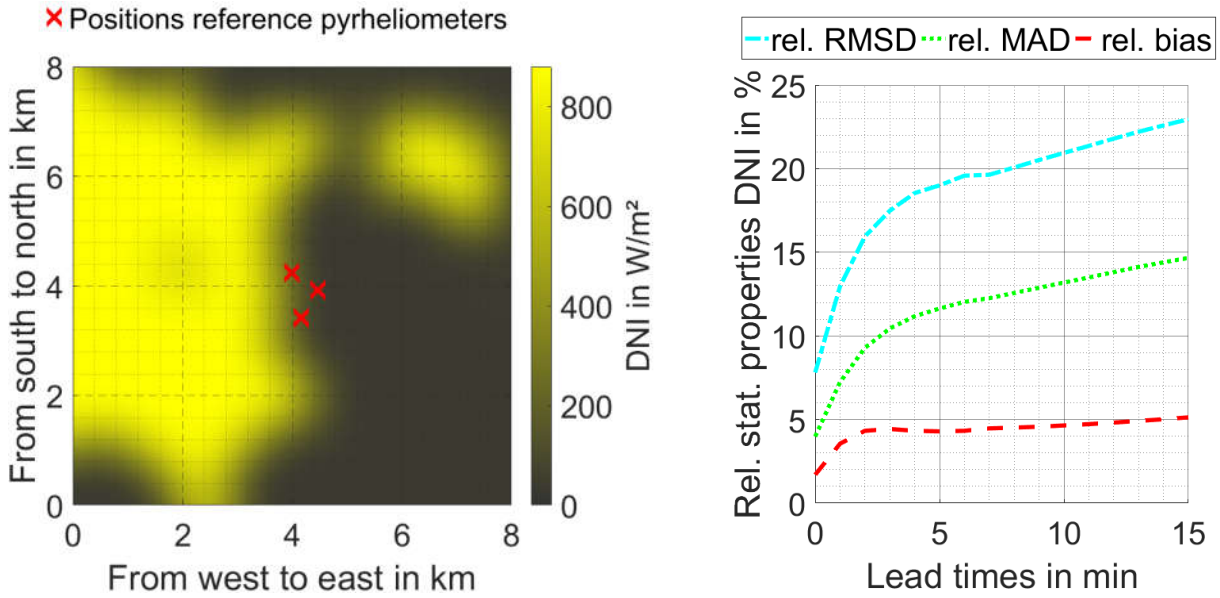

Figure 12: (Left) Example DNI map with marked positions of reference pyrheliometers (Right) Relative statistics of irradiance maps validation with three reference pyrheliometer including the years 2016 and 2017.

The comparison of nowcasting validation results is a difficult task, due to the complex and variable nature of the processes within the earth's atmosphere. The results of the same system may vary strongly during different ambient conditions. For the comparison of systems, often the skill score is used (**Marquez & Coimbra 2013**). The skill score given as

$$s = 1 - RMSD_N / RMSD_P$$ **Equation 2**

428 whereas $RMSD_N$ describes the investigated nowcasting system and $RMSD_P$ a corresponding
429 persistence forecast. The overall system skill score over the entire data set is shown in Figure
430 13 (blue line). The skill score drops from lead time 1 to lead time 15 from around 0.11 to 0.01.
431 However, the chosen validation data set has also a strong impact on the skill score. As we
432 shown in this work as well as previous publications (**Nouri et al. 2019)**, will ASI based
433 nowcasting deviations rise in the case of multi-layer conditions including middle and high layer
434 clouds, compared to more simple single layer conditions with low layer clouds. The orange line
435 of Figure 13 shows the skill score, when 10% of the days are filtered. These filtered days include
436 multi-layer conditions with middle and high layer clouds. We observe a skill score improvement
437 of up to 10%. The comparison of two example days shows this even more clearly. The yellow
438 curve of Figure 13 shows the skill score of a complex multi-layer day with stratus/altostratus as
439 well as cirrus/cirrostratus clouds. The persistence forecast outperformance the presented
440 nowcasting system on this day. On the contrary, on a single layer day with cumulus clouds,
441 outperformance the presented nowcasting system clearly the persistence forecast (see purple

curve of Figure 13). The DNI curves of both example days are illustrated in Figure 14.

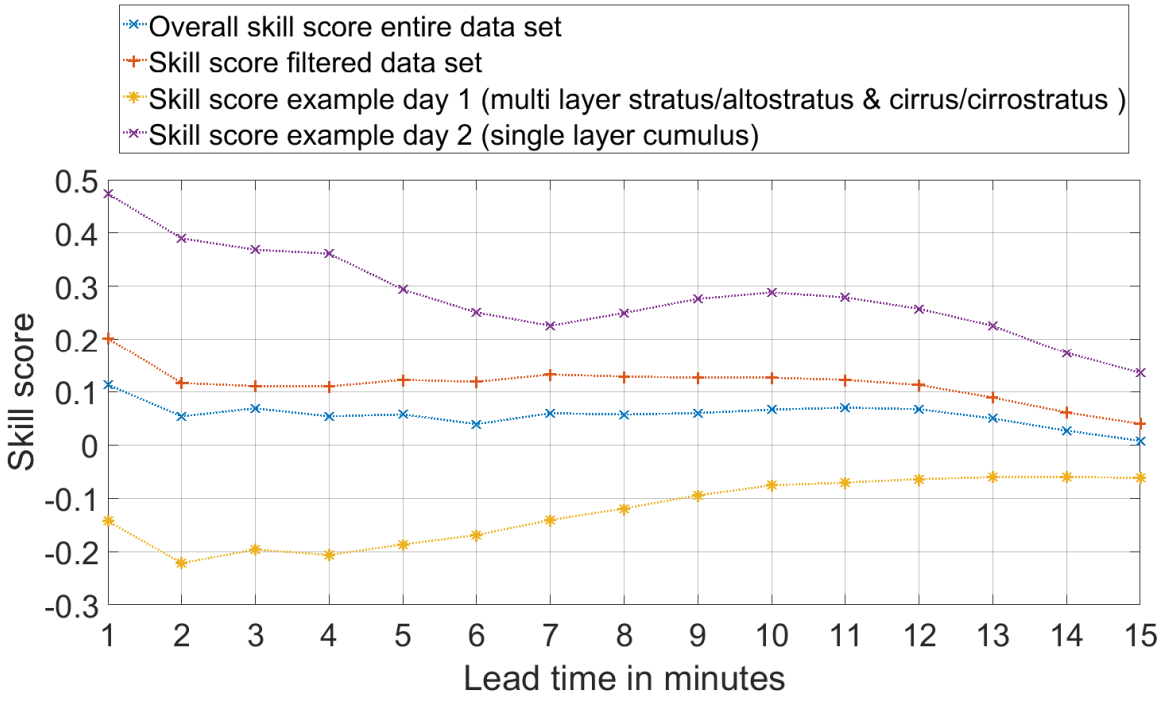

Figure 13: Skill score of entire data set (blue), filtered data set without 10 % of the most complex days (multi-layer including high layer clouds)(orange), complex example day with multi-layer stratus/altostratus & cirrus/cirrostratus clouds (yellow) and simple day with single layer cumulus clouds (purple)

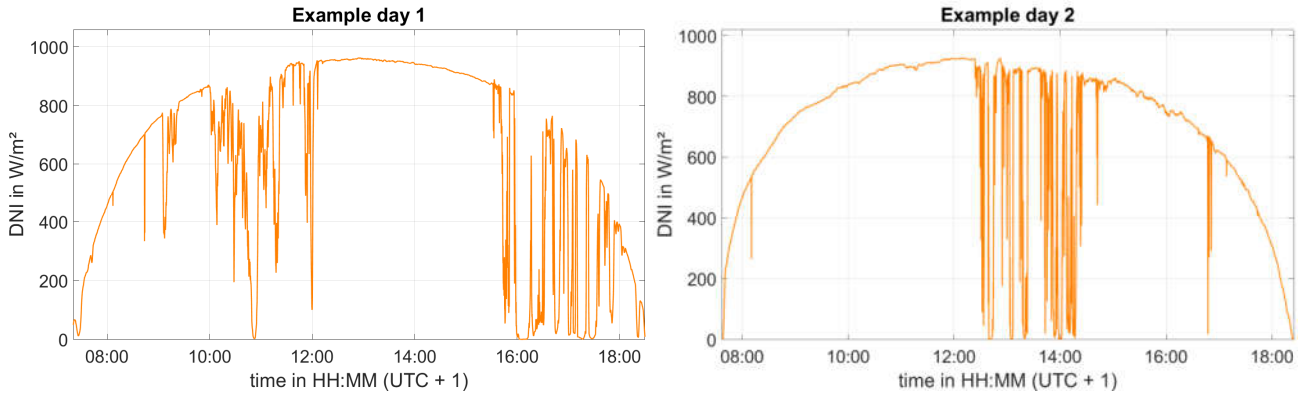

Figure 14: DNI curves of example days (Left) example day 1 with complex multi-layer stratus/altostratus & cirrus/cirrostratus clouds (Right) simple day with single layer cumulus clouds

5 Site dependencies and the potential of automatic cloud classification

5.1 Discussing site dependence

The transmittance estimation approach presented here uses a probabilistic look-up table generated for and corresponding to the local conditions of PSA. Other sites might have different statistical relationships between the distribution of cloud transmittance and height. Especially latitude dependencies regarding e.g. cloud height related moisture and cloud type distributions must be taken into account (**Manabe 1969; Ohring & Adler 1978; Sassen & Wang 2012**). Deviations in cloud type distribution, despite equal latitude, occur due to local meteorological conditions. Furthermore, the occurrence of low layer clouds is higher in the southern hemisphere compared to the northern hemisphere, probably due to the larger proportion of ocean surfaces (**Stubenrauch et al. 2006**). Seasonal or diurnal dependencies of the cloud distribution (**Stubenrauch et al. 2006**) are currently not considered.

However, the described approach always includes recent cloud transmittance measurements belonging to the actual site and uses the results of the probability analysis as weighting factors if several measured values can be considered. During operation the cloud transmittance measurements and the corresponding height measurements taken by the nowcasting system are saved into a database. Thus, the PSA probability data base is gradually improved and finally replaced by measurements belonging to the new site, improving the nowcasting quality with time.

5.2 Potential of cloud classification for improving cloud transmittance estimations

Objective visual classification of clouds with its strong variation of micro- and macrophysical properties is a difficult task. A bias depending on the experience and preferences of the user is unavoidable. However, various groups developed cloud classification approaches from ASI images (e.g. **Heinle et al. 2010; Kazantzidis e al. 2012; Wacker et al. 2015; Huertas-Tato et al. 2017**). All of the mentioned groups use approaches with machine learning algorithms, such as the k-nearest neighbor's or random forests algorithm. In most cases up to seven cloud types are considered, including clear sky, cumulus, stratus/altostratus, stratocumulus, cirrocumulus/altocumulus, cirrus/cirrostratus and cumulonimbus/nimbostratus (**Heinle et al. 2010**). **Huertas-Tato et al. 2017** added the class multicloud, which does not distinguish between different cloud types, but indicates if more than one cloud type is present.

The cloud classification approaches from ASIs achieve high accuracies with correct hit rates around 90% for single-layer conditions (see Table 3). However, the accuracies drop significantly with random data sets including multi-layer conditions (**Wacker et al. 2015**).

487 **Table 3: Some published average cloud classification accuracies**

	Average hit rate	
	Single-layer conditions	Single & Multi-layer conditions
Heinle et al. 2010	87.52%	n/a
Kazantzidis e al. 2012	87.90%	n/a
Wacker et al. 2015	91.70%	Down to ≈ 50%
Huertas-Tato et al. 2017	77.3%	72.60%(*)

(*) Including multicloud class without further specification of the present cloud classes

488 An accurate automatic cloud classification from the ASI images is expected to further improve
489 the transmittance estimation approach described in section 3. The site dependency issue during
490 the initial phase at a new site could be reduced by linking transmittance measurements directly
491 to the cloud type rather than cloud height. Furthermore, the distinction between different middle
492 layer cloud types with liquid dominated Ac and ice dominated As clouds would be helpful,
493 although the optical cloud properties from the same cloud class remain variable especially for
494 middle layer clouds (**Sassen & Wang 2012**; **Kayetha & Collins 2016**). To estimate the potential
495 improvement, we manually classified 10% of the transmittance validation data set, introduced in
496 section 4. The data selection considers 10% of each day, within a day the data is chosen
497 randomly. Thus, no bias is introduced due to the data selection. Only the clouds which mask the
498 sun from the perspective of the ASI are classified. We use the cloud classes cumulus,
499 stratus/altostratus, stratocumulus, cirrocumulus/altocumulus and cirrus/cirrostratus according to
500 **Heinle et al. 2010**. Situations with cumulonimbus/nimbostratus, which seldom occur at PSA, are
501 rejected. The transmittance validation data set includes no clear sky conditions. Multi-layer
502 conditions are accepted, as long as the cloud covering the sun (ASI perspective) is clearly
503 distinguishable/classifiable. The transmittance of each manually classified cloud is known, thus
504 we discretized transmittance ranges over cloud classes. The relative occurrence of

transmittance ranges within cloud classes is shown in Figure 15. Different colors refer to different transmittance ranges. Rather unambiguous results exist for predominantly optically thick cumulus and stratocumulus as well as predominantly thin cirrus/cirrostratus clouds. A strong dispersion is visible for the cloud classes stratus/altostratus as well as cirrocumulus/altocumulus. In particular the combined class, including low layer stratus and middle layer altostratus clouds, is unfavorable for the transmittance determination. A slightly different classification scheme is recommended to be combined with the cloud height base approach, distinguishing between separate stratus and altostratus as well as cirrocumulus and altocumulus clouds. However, the results shown in Figure 15 show a good agreement with the results of the probability analysis (section 3.1) as well as the validation of the transmittance estimation (section 4.1).

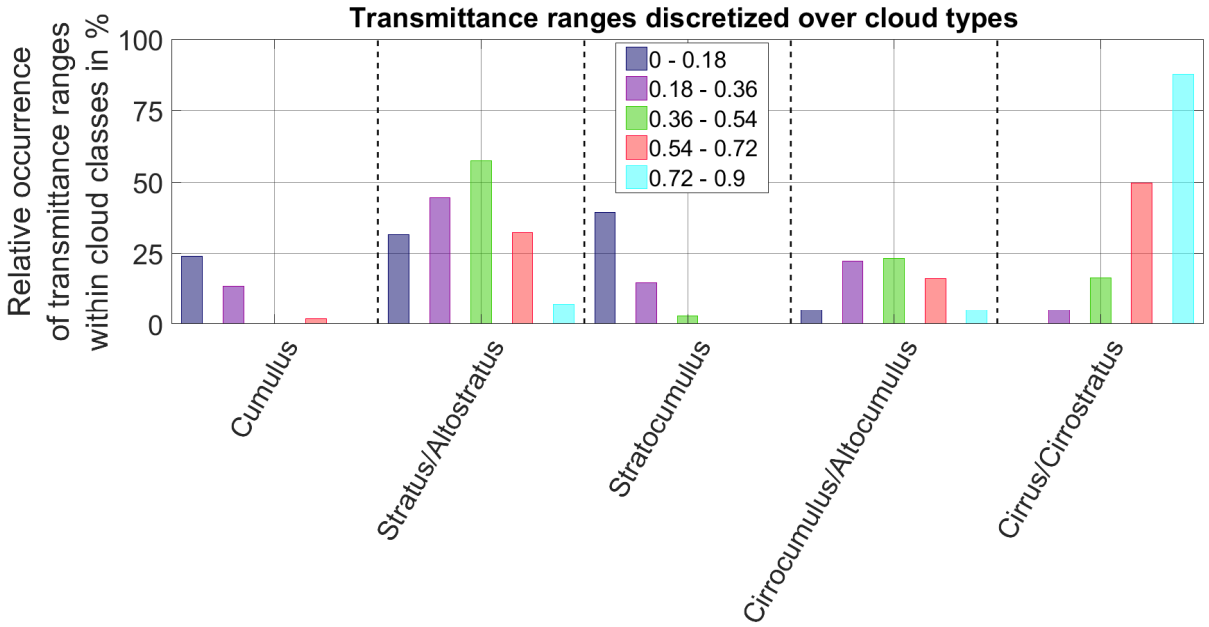

Figure 15: Relative occurrence of transmittance ranges within cloud classes (manually classified). Different colors refer to different transmittance ranges. All bars of the same transmittance range add up to 100%.

6 Conclusion and outlook

We presented a method to determine cloud transmittance with a cloud object based solar irradiance nowcasting system consisting of multiple ASIs and a pyrheliometer (**Nouri et al. 2018**). Each detected cloud object receives a cloud height, determined by a stereoscopic method (**Nouri et al. 2019**). Some of the cloud objects receive transmittance measurements, acquired by the pyrheliometer. The remaining cloud objects need transmittance estimations. A novel probabilistic approach has been developed, correlating cloud transmittance measurements and cloud height measurements. We developed a transmittance estimation approach (suitable for real-time operation), which calculates a weighted average transmittance from recent transmittance measurements with corresponding cloud heights. The weighting factors are defined by the average probability of transmittance values within the corresponding height range. Transmittance and accurate ceilometer cloud height measurements from 574 cloudy days distributed over the years 2014 to 2017 were analyzed. The results of the probability analysis show a clear correlation between low layer optically thick clouds and high layer optically thin clouds. Middle layer clouds are ambiguous with a strong dispersion from optically thin to optically thick clouds. This was to be expected, due to the micro- and macrophysical properties of middle layer clouds (**Sassen & Wang 2012**; **Kayetha & Collins 2016**). Nevertheless the presented validation of the transmittance estimation procedure, over the entire years 2016 and 2017, reached an overall MAD and RMSD of 0.11 and 0.16 respectively. We compared the probabilistic transmittance estimation approach with two binary, a simple statistical and a persistence approach. The probabilistic approach outperforms clearly all of them.

Three ground based pyrheliometer stations were used to validate the overall DNI forecast according to **Kuhn et al. 2017**. Over the two years validation period a relative bias, MAD and RMSD of 2%, 4% and 8% respectively were found for a lead time of 0 minutes. The deviation metrics rise up to 5%, 15% and 23% respectively for a lead time of 15 minutes ahead. Cloud tracking and transmittance estimation uncertainties, are the main cause for increased deviation with higher lead times. The increase of the deviations with higher lead times are dominated by a steep rise within the first four minutes, then the deviation metrics curves flatten out. This is due to the fact that in the case of low lead times actual transmittance measurements are frequently available for the relevant clouds. For higher lead times the transmittance values of the relevant clouds are in almost all cases estimated values.

Of course the validation results are affected by the chosen data set. The performance of nowcasting system will vary under different conditions. We discuss the influence of complex multi-layer conditions compared to more homogeneous single-layer on the skill score. We conclude that the comparison from nowcasting system on the basis of different data sets remains a difficult task.

The site dependence of the presented approach was discussed. The cloud height and transmittance distribution of the used probability analysis represents the conditions at PSA. However, new cloud transmittance and height measurements of a new site will substitute with time the PSA data and thus improve the system accuracy

ASI based cloud classifications could improve the transmittance estimation and reduce the site dependence. However, a system improvement requires particularly high classification accuracies with middle layer clouds and multi-layer conditions. Currently the highest classification inaccuracies are found with stratus/altostratus and cirrocumulus/altocumulus

(**Wacker et al. 2015**) as well as multi-layer conditions (**Wacker et al. 2015; Huertas-Tato et al. 2017**). These are precisely the conditions, in which also the probabilistic approach shows the highest deviations. Furthermore the relationships between cloud type and transmittance for the cloud classes stratus/altostratus and cirrocumulus/altocumulus, which include the middle layer clouds, are as expected ambiguous. A simplified classification could be conceivable, which discretizes the cloud cover in optically thin and optically thick clouds within the cloud height ranges. This would be also a first step away from clouds with homogenous optical properties to more realistic clouds with both horizontal and vertical variability.

ASI based nowcasting systems harbor a great potential for energy, meteorology and atmospheric sciences and industry. The correct assessment of the transmittance of clouds is one of the main challenges that have to be mastered. The presented approach can be used to estimate the transmittance for such nowcasting systems.

Acknowledgment

This research has received funding from the European Union's FP7 Programme under Grant Agreement no. 608623 (DNICast project) and the German Federal Ministry for Economic Affairs and Energy within the WobaS project.

References

Bar-Or, R. Z., Koren, I., Altaratz, O., 2010. Estimating cloud field coverage using morphological analysis, Environ. Res. Lett., 5(1), 014022. doi:10.1088/1748-9326/5/1/014022.

Blanc, P., Massip, P., Kazantzidis, A., Tzoumanikas, P., Kuhn, P., Wilbert, S., Schüler, D., Prahl, C., 2017. Short-term forecasting of high resolution local DNI maps with multiple fish-eye cameras in stereoscopic mode. AIP Conf. Proc. 1850 (1), 140004. doi: 10.1063/1.4984512.

Breyer, C., Bogdanov, D., Gulagi, A., Aghahosseini, A., Barbosa, L., Koskinen, O., Barasa, M., Caldera, U., Afanasyeva, S., Child, M., Farfan, J., Vainikka, P., 2017. On the role of solar photovoltaics in global energy transition scenarios. Progr. Photovoltaics 25, 727–745. doi: 10.1002/pip.2885

Chang, F.-L., and Z. Li, 2002: Estimating the vertical variation of cloud droplet effective radius using multispectral nearinfrared satellite measurements. J. Geophys. Res., 107, 4257, AAC 7-1-AAC 7-12. doi:10.1029/2001JD000766.

Chen, J., Rossow, W. B., Zhang, Y., 2000. Radiative effects of cloud-type variations. J. Climate, 13, 264–286. doi: 10.1175 1520 0442 2000 013 0264 REOCTV 2.0 CO 2

601

602 Chen, X., Du, Y., Wen, H., 2017. Forecasting based power ramp-rate control for PV systems
603 without energy storage. In: 2017 IEEE 3rd International Future Energy Electronics Conference
604 and ECCE Asia (IFEEC 2017 - ECCE Asia), pp. 733–738. doi: 10.1109/IFEEC.2017.7992130

605

606 Chow, C.W., Urquhart, B., Lave, M., Dominguez, A., Kleissl, J., Shields, J., Washom, B., 2011.
607 Intra-hour forecasting with a total sky imager at the UC San Diego solar energy testbed. Solar
608 Energy 85, 2881–2893. doi: 10.1016/j.solener.2011.08.025

609

610 Chow, C.W., Belongie, S., Kleissl, J., 2015. Cloud motion and stability estimation for intra-hour
611 solar forecasting. Solar Energy 115, 645–655. http://dx.doi.org/10.1016/j.solener.2015.03.030.

612

613 Frederick, J. E., Steele, H. D., 1995. The transmission of sunlight through cloudy skies: An
614 analysis based on standard meteorological information. J. Appl. Meteor., 34, 2755–2761. doi:
615 10.1175/1520-0450(1995)034<2755:TTOSTC>2.0.CO;2

616

617 Fu Q., 1996. An accurate parameterization of the solar radiative properties of cirrus clouds for
618 climate models. J Climate;9:2058–82. doi: 10.1175/1520-
619 0442(1996)009<2058:AAPOTS>2.0.CO;2

620

621

622 Geuder, N., Wolfertstetter, F., Wilbert, S., Schüler, D., Affolter, R., Kraas, B., Lüpfert, E.,
623 Espinar, B., 2015. Screening and Flagging of Solar Irradiation and Ancillary Meteorological Data,
624 Energy Procedia, 69, 1989–1998. doi:10.1016/j.egypro.2015.03.205, 2015.

625

626 Hahn, C. J., Rossow, W. B., Warren, S. G., 2001. ISCCP cloud properties associated with
627 standard cloud types identified in individual surface observations. J. Climate, 14, 11–28. doi:
628 10.1175/1520-0442(2001)014<0011:ICPAWS>2.0.CO;2

629

630 Hanrieder, N., Sengupta, M., Xie, Y., Wilber, S., Pitz-Paal, R., 2016. Modeling beam attenuation
631 in solar tower plants using common DNI measurements. Solar Energy 129, pp. 244-255. doi:
632 10.1016/j.solener.2016.01.051

633

634 Heinle, A., Macke, A., Srivastav, A., 2010. Automatic cloud classification of whole sky images,
635 Atmos. Meas. Tech. 3 (2010) 557-567. doi: 10.5194/amt-3-557-2010

636

637 Hess, M., Koepke, P., Schult, I., 1998. Optical properties of aerosols and clouds: The software
638 package OPAC. Bull. Amer. Meteor. Soc, 79, 831–844. doi: 10.1175/1520-
639 0477(1998)079<0831:OPOAAC>2.0.CO;2

640

641 Hirsch, T., Martin, N., Gonzalez. L., Biencinto, M., Wilbert, S., Schroedter-Homscheidt, M.,
642 Chenlo, F., Feldhoff, J., 2014. Direct Normal Irradiance Nowcasting methods for optimized
643 operation of concentrating solar technologies, DNICast project, DNIcast Deliverable 2.1.
644 http://www.dnicast-project.net

645

646 Hong, Y., Liu, G., Li, J.-L. F., 2016. Assessing the Radiative Effects of Global Ice Clouds Based
647 on CloudSat and CALIPSO Measurements, J. Climate, 29, 7651–7674. doi:10.1175/JCLI-D-15-
648 0799.1

649

650 Huang, H., Yoo, S., Yu, D., Huang, D., Qin, H., 2012. Correlation and local feature based cloud
651 motion estimation. In: Proceedings of the Twelfth International Workshop on Multimedia Data
652 Mining. MDMKDD ’12. ACM, New York, NY, USA, pp. 1–9. doi: 10.1145/2343862.2343863 .

653

654 Huertas-Tato, J., Rodríguez-Benítez, F.J., Arbizu-Barrena, C., Aler-Mur, R., Galvan-Leon, I.,
655 Pozo-Vázquez, D., 2017. Automatic cloud-type classification based on the combined use of a
656 sky camera and a ceilometer. J. Geophys. Res. Atmos. 122, 11045–11061. doi:
657 10.1002/2017JD027131

658

659 Ineichen, P., Perez, R., 2002. A new airmass independent formulation for the Linke turbidity
660 coefficient. Solar Energy 73, pp. 151-157. doi: 10.1016/S0038-092X(02)00045-2

661

662 Inman, R.H., Pedro, H.T.C., Coimbra, C.F.M., 2013. Solar forecasting methods for renewable
663 energy integration. Prog. Energy Combust. Sci. 39, 535–576. doi: 10.1016/j.pecs.2013.06.002.

664

665 Kahn, B.H., Chahine, M.T., Stephens, G.L., Mace, G.G., Marchand, R.T., Wang, Z., Barnet,
666 C.D., Eldering, A., Holz, R.E., Kuehn, R.E., Vane, D.G., 2008. Cloud type comparisons of AIRS,
667 CloudSat, and CALIPSO cloud height and amount, Atmos. Chem. Phys., 8, 1231-1248. doi:
668 10.5194/acp-8-1231-2008.

669

670 Kayetha, V.K., Collins, R.L., 2016. Optically thin midlevel ice clouds derived from Cloud Aerosol
671 Lidar and Infrared Pathfinder Satellite Observations, J. Appl. Remote Sens. 10(4), 046007. doi:
672 10.1117/1.JRS.10.046007.

673

674 Kazantzidis, A., Tzoumanikas, P., Bais, A.F., Fotopoulos, S., Economou, G., 2012. Cloud
675 detection and classification with the use of whole-sky ground-based images, Atmos. Res. 113
676 80-88. doi: 10.1016/j.atmosres.2012.05.005

677

678 Kazantzidis, A., Tzoumanikas, P., Blanc, P., Massip, P., Wilbert, S., Ramirez-Santigosa, L.,
679 2017. 5 - short-term forecasting based on all-sky cameras. In: Kariniotakis, G. (Ed.), Renewable
680 Energy Forecasting. Woodhead Publishing Series in Energy. Woodhead Publishing, pp. 153–
681 178. doi: 10.1016/B978-0-08-100504-0.00005-6

682

683 Kikuchi, N., Nakajima, T., Kumagai, H., Kuroiwa, H., Kamei, A., Nakamura, R., Nakajima, T. Y.,
684 2006. Cloud optical thicness and effective particle radius derived from transmitted solar radiation
685 measurements: comparison with cloud radar observations, J. Geophys. Res. 111, D07205.
686 doi:10.1029/2005JD006363

687

688 King, M. D., 1987. Determination of the scaled optical thickness of clouds from reflected solar
689 radiation measurements. J. Atmos. Sci., 44, 1734–1751. doi: 10.1175/1520-
690 0469(1987)044<1734:DOTSOT>2.0.CO;2

691

692 Kokhanovsky A. 2004. Optical properties of terrestrial clouds. Earth Sci Rev 2004;64:189–241.
693 doi: 10.1016/S0012-8252(03)00042-4

694

695 Koren, I., Remer, L.A., Kaufman, Y.J., Rudich, Y., Martins, J.V., 2007. On the twilight zone
696 between clouds and aerosols Geophys. Res. Lett. 34 L08805. doi: 10.1029/2007GL029253

697

698 Kuhn, P., Nouri, B., Wilbert, S., Prahl, C., Kozonek, N., Schmidt, T., Yasser, Z., Ramirez, L.,
699 Zarzalejo, L., Meyer, A., Vuilleumier, L., Heinemann, D., Blanc, P., Pitz-Paal, R., 2017.
700 Validation of an all-sky imager-based nowcasting system for industrial PV plants. Prog.
701 Photovolt.: Res. Appl. doi: 10.1002/pip.2968.

705

706 Li, J., Yi, Y., Minnis, P., Huang, J., Yan, H., Ma, Y., Wang, W., Ayers, J.K., 2011. Radiativeeffect
707 differences between multilayered and single-layer clouds derived from CERES, CALIPSO, and
708 CloudSat data. J. Quant. Spectrosc. Radiat. Transfer, 112, 361–375. doi:
709 10.1016/j.jqsrt.2010.10.006

710

711 Lohmann, U., Neubauer, D., 2018. The importance of mixed-phase and ice clouds for climate
712 sensitivity in the global aerosol–climate model ECHAM6-HAM2, Atmos. Chem. Phys., 18, 8807–
713 8828. doi: 10.5194/acp-18-8807-2018

714

715 Lorenz, E., Remund, J., Müller, S., Traunmüller, W., Steinmaurer, G., Pozo, D., Ruiz-Arias, J.,
716 Fanego, V., Ramirez, L., Romeo, M., Kurz, C., Pomares, L., Guerrero, C., 2009. Benchmarking
717 of different approaches to forecast solar irradiance. 24th European Photovoltaic Solar Energy
718 Conference, Hamburg, Germany, 21–25.

719

720 Madhavan, B. L., Kalisch, J., Macke, A., 2016. Shortwave surface radiation network for
721 observing small-scale cloud inhomogeneity fields, Atmos. Meas. Tech., 9, 1153–1166.
722 doi:10.5194/amt-9- 1153-2016

723

724 Manabe, J., 1969. Climate and the ocean circulation I. The atmospheric circulation and the
725 hydrology of the earth surface. Mon. Wea. Rev., 97, 739-774. doi: 10.1175/1520-
726 0493(1969)097<0775:CATOC>2.3.CO;2

727

728 Marquez, R., Coimbra, C. F., 2013. Proposed metric for evaluation of solar forecasting models.,
729 Journal of solar energy engineering, 135(1). doi: 10.1115/1.4007496

730

731 Mejia, F. A., Kurtz, B., Murray, K., Hinkelman, L. M., Sengupta, M., Xie, Y., Kleissl, J., 2016.
732 Coupling sky images with radiative transfer models:A new method to estimate cloud optical
733 depth, Atmos. Meas. Tech., 9, 4151–4165. doi:10.5194/amt-9-4151-2016.

734

735 Noureldin, K., Hirsch, T., Kuhn, P., Nouri, B., Yasser, Z., Pitz-Paal, R., 2017. Modelling an
736 Automatic Controller for Parabolic Trough Solar Fields under Realistic Weather Conditions, 23rd
737 SolarPACES Conference

738

739 Nouri, B., Kuhn, P., Wilbert, S., Prahl, C., Pitz-Paal, R., Blanc, P., Schmidt, T., Yasser, Z.,
740 Ramirez Santigosa, L., Heineman, D., 2018. Nowcasting of DNI Maps for the Solar Field Based
741 on Voxel Carving and Individual 3D Cloud Objects from All Sky Images, AIP Conference
742 Proceedings. Vol. 2033. doi:10.1063/1.5067196

743

744 Nouri, B., Kuhn, P., Wilbert, S., Hanrieder, N., Prahl C., Zarzalejo, L., Kazantzidis, A., Blanc, P.,
745 Pitz-Paal, R., 2019, Cloud height and tracking accuracy of three all sky imager systems for
746 individual clouds . Sol. Energy 177, 213–228. doi: 10.1016/j.solener.2018.10.079

747

748 Nguyen, D.A., Kleissl, J., 2014. Stereographic methods for cloud base height determination
749 using two sky imagers. Solar Energy 107, 495–509. doi: 10.1016/j.solener.2014.05.005.

750

751 Ohring, G., Adler, S., 1978. Some experiments with a zonally-averaged climate model, Journal
752 of Atmospheric Science. 35, 186–205. doi: 10.1175/1520-
753 0469(1978)035<0186:SEWAZA>2.0.CO;2

754

755 Perez, R., David, M., Hoff, T.E., Jamaly, M., Kivalov, S., Kleissl, J., Lauret, P., Perez, M., 2016.
756 Spatial and temporal variability of solar energy. Found. Trends Renew. Energy 1 (1), 1–44. doi:
757 10.1561/2700000006

758

759 Pruppacher, R. H., Klett, J. D., 1997. Microphysics of Clouds and Precipitation. 2nd ed.
760 Atmospheric and Oceanographic Sciences Library, Vol. 18, Kluwer Academic Publishers, ISBN
761 978-0-306-48100-0

762

763 Raschke, R.A., Cox, S.K., 1983. Instrumentation and technique for deducing cloud optical
764 thickness. J. Clim. Appl. Meteorol. 22 (11), 1887 – 1893. doi: 10.1175/1520-
765 0450(1983)022<1887:IATFDC>2.0.CO;2

766

767 Richardson, W., Krishnaswami, H., Vega, R., Cervantes, M., 2017. A Low Cost, Edge
768 Computing, All-Sky Imager for Cloud Tracking and Intra-Hour Irradiance Forecasting.
769 Sustainability 2017. 9(4). 482. doi: 10.3390/su9040482

770

771 Rossow, W. B., Schiffer, R. A., 1999. Advances in understanding clouds from ISCCP. Bull.
772 Amer. Meteor. Soc., 80, 2261-2287. doi: 10.1175/1520-0477(1999)080<2261:AIUCFI>2.0.CO;2

773

780 Sassen, K., Wang, Z., 2012. The clouds of the middle troposphere: Composition, radiative
781 impact, and global distribution, Surv.Geophys., 33(3–4), 677–691. doi:10.1007/s10712-011-
782 9163-x.

783

784 Schmidt, T., Kalisch, J., Lorenz, E., Heinemann, D., 2016. Evaluating the spatio-temporal
785 performance of sky-imager-based solar irradiance analysis and forecasts. Atmos. Chem. Phys.
786 16, 3399–3412. doi: 10.5194/acp-16-3399-2016.

787

788 Schroedter-Homscheidt, M., Gesell, G., 2016. Verification of sectoral cloud motion based direct
789 normal irradiance nowcasting from satellite imagery, AIP Conf. Proc. 1734, 150007. doi:
790 10.1063/1.4949239

791

792 Schroedter-Homscheidt, M., Kosmale, M., Jung, Sandra., Kleissl, Jan., 2018. Classifying
793 ground-measured 1 minute temporal variability within hourly intervals for direct normal
794 irradiances, Meteorol. Z., doi: 10.1127/metz/2018/0875

795

796 Stubenrauch, C. J., Chedin, A., Rädel, G., Scott, N.A. Serrar, S., 2006. Cloud properties and
797 their seasonal and diurnal variability from TOVS Path-B. J. Climate, 19, 5531–5553. doi:
798 10.1175/JCLI3929.1

799

800 Sun, Z., Shine, K. P., 1994. Studies of the radiative properties of ice and mixed-phase clouds.
801 Quart. J. Roy. Meteor. Soc., 120, 111–137. doi: 10.1002/qj.49712051508

802

803 Taravat, A., Frate, F. D., Cornaro, C., Vergari, S., 2015. Neural Networks and Support Vector
804 Machine Algorithms for Automatic Cloud Classification of Whole-Sky Ground-Based Images,
805 IEEE Geoscience and Remote Sensing Letters 12(3), 666–670. doi: 10. 1109/ LGRS. 2014.
806 2356616

807

808 Titov, G. A., 1998. Radiative horizontal transport and absorption in stratocumulus clouds.
809 Journal of the Atmospheric Sciences, 55, 2549 – 2560. doi: 10.1175/1520-
810 0469(1998)055<2549:RHTAAI>2.0.CO;2

811

812 Tzoumanikas, P., Nikitidou, E., Bais, A.F., Kazantzidis, A., 2016. The effect of clouds on surface
813 solar irradiance, based on data from an all-sky imaging system, Renew. Energy 95, 314-322.
814 doi: 10.1016/ j.renene.2016.04.026.

815

816 Wacker, S., Grobner, J., Zysset, C., Diener, L., Tzoumanikas, P., Kazantzidis, A., Vuilleumier,
817 L., Stockli, R., Nyeki, S., Kämpfer, N., 2015. Cloud observations in Switzerland using
818 hemispherical sky cameras, J. Geophys. Res. Atmos. 120. doi: 10.1002/2014JD022643.

819

820 Wang, J., Rossow, W., Zhang, Y., 2000. Cloud Vertical Structure and Its Variations from a 20-Yr
821 Global Rawinsonde Dataset. J. Clim. 13, 3041 – 3056. doi: 10.1175/1520-
822 0442(2000)013<3041:CVSAIV>2.0.CO;2

823

824 Wang, Z., Sassen, K., 2001. Cloud type and macrophysical property retrieval using multiple
825 remote sensors. /. Appl. Meteor., 40, 1665-1682. doi: 10.1175/1520-
826 0450(2001)040<1665:CTAMPR>2.0.CO;2

827

828 West, SR., Rowe, D., Sayeef, S., Berry, A., 2014. Short-term irradiance forecasting using
829 skycams: motivation and development. Sol. Energy. 110. 188-207.
830 http://dx.doi.org/10.1016/j.solener.2014.08.038.

831

832 Wilbert, S., Nouri, B., Prahl, C., Garcia, G., Ramirez, L., Zarzalejo, L., Valenzuela, L., Ferrera,
833 F., Kozonek, N., Liria, J., 2016a. Application of Whole Sky Imagers for Data Selection for
834 Radiometer Calibration. In: EU PVSEC 2016 Proceedings, 1493–1498. doi:
835 10.4229/EUPVSEC20162016-5AO.8.6

836

837 Wilbert, S., Kleindiek, S., Nouri, B., Geuder, N., Habte, A., Schwandt, M., Vignola, F., 2016b.
838 Uncertainty of rotating shadowband irradiometers and Si-pyranometers including the spectral
839 irradiance error. AIP Conference Proceedings 1734. doi: 10.1063/1.4949241

840

841 Ye, L., Cao, Z., Xiao, Y., 2017. DeepCloud: Ground-Based Cloud Image Categorization Using
842 Deep Convolutional Features, IEEE Transactions on Geoscience and Remote Sensing 55(10),
843 5729–5740. doi: 10.1109/TGRS.2017.2712809

844

845 Zangvil, A., Lamb P.J., 1997. Characterization of sky conditions by the use of solar radiation
846 data Solar Energy,61, pp. 17-22. doi: 10.1016/S0038-092X(97)00035-2

847